Available online at www.sciencedirect.com
SCIENCE DIRECT®
Acta Materialia 52 (2004) 749–764
Acta MATERIALIA
www.actamat-journals.com

Phase field simulations of ferroelectric/ferroelastic polarization switching

Jie Wang [a], San-Qiang Shi [b], Long-Qing Chen [c], Yulan Li [c], Tong-Yi Zhang [a,*]

[a] *Department of Mechanical Engineering, Hong Kong University of Science and Technology, Clear Water Bay, Kowloon, Hong Kong, China*
[b] *Department of Mechanical Engineering, Hong Kong Polytechnic University, Hong Kong, China*
[c] *Department of Materials Science and Engineering, The Pennsylvania State University, University Park, PA 16802, USA*

Received 18 July 2003; received in revised form 28 September 2003; accepted 7 October 2003

Abstract

Polarization switching in a ferroelectric subjected to an electric field or a stress field is simulated using a phase-field model based on the time-dependent Ginzburg–Landau equation, which takes both multiple-dipole–dipole–electric and multiple-dipole–dipole–elastic interactions into account. The temporal evolution of the polarization switching shows that the switching is a process of nucleation, if needed, and growth of energy-favorite domains. Macroscopic polarization and strain are obtained by averaging polarizations and strains over the entire simulated ferroelectric. The simulation results successfully reveal the hysteresis loop of macroscopic polarization versus the applied electric field, the butterfly curve of macroscopic strain versus the applied electric field, and the macroscopically nonlinear strain response to applied compressive stresses.

Keywords: Phase-field models; Phase transformation; Simulation; Ferroelectricity; Microstructure

1. Introduction

Ferroelectric materials have become preferred materials in a wide variety of electronic and mechatronic devices due to their pronounced dielectric, piezoelectric, and pyroelectric properties. These distinct dielectric, piezoelectric, and pyroelectric properties are related to ferroelectric domain structures and polarization switching. If one can design, fabricate, and/or control the domain structures and polarization switching, one should be able to take full advantage of ferroelectric materials in manufacturing modern electronic and mechatronic devices. It is therefore of great importance to understand and predict the ferroelectric domain structures and polarization switching when such materials are subjected to external electrical and/or mechanical loading.

A ferroelectric material possesses spontaneous polarization, spontaneous strain and a domain structure below its Curie temperature. The spontaneous strain is a measure of the lattice distortion induced by the spontaneous polarization. Due to the crystalline anisotropy, the direction of the spontaneous polarization in a lattice cell is along one of the polar axes in the crystal. An electric domain represents a region in which all lattice cells have the same polarizations. A domain structure of a ferroelectric consists of domains with different orientations and boundaries between the domains, which are called domain walls. Sufficiently high electrical and/or mechanical fields can switch polarizations by 180° or about 90° from one polar axis to another and thus result in domain nucleation, domain wall motion, domain switching and/or a complete change in the domain structure. In an electrical field-loaded ferroelectric, the macroscopic polarization switches 180° and causes a hysteresis loop of polarization versus the electric field and an associated butterfly loop of strain versus the electric field when the applied electric field reverses its direction. Switching a polarization by 180° causes little

---

[*] Corresponding author. Tel.: +852-235-87192; fax: +852-235-815-43.
E-mail address: mezhangt@ust.hk (T.-Y. Zhang).

1359-6454/$30.00 © 2003 Acta Materialia Inc. Published by Elsevier Ltd. All rights reserved.
doi:10.1016/j.actamat.2003.10.011

or no mechanical distortion because the spontaneous strain has a 180°-symmetry, whereas 90°-polarization switching involves a change in the orientation of the spontaneous strain by about 90° and thus changes internal stresses. Clearly, the macroscopic behavior of a ferroelectric under applied electrical and/or mechanical loading is a statistically averaged response over entire polarizations of crystalline cells.

Many theoretical studies have been conducted to understand and predict the nonlinear behavior caused by polarization switching [1–17]. Thermodynamic approaches are usually used to establish switching criteria and the switching region is usually assumed to be a domain. For example, a thermodynamic energy-based criterion for an individual domain states that a domain switches when the electric work plus the mechanical work exceed a critical value [8]. According to the criterion, 180°-switching, where stresses are irrelevant, is activated if

$$E_i \Delta P_i \geqslant 2P_s E_c, \tag{1}$$

where E_i and P_i are the electric field strength and the polarization vectors, respectively, P_s is the magnitude of the spontaneous polarization, E_c is the absolute value of the coercive field, and the Δ denotes a change of a property before and after the switching. With 90°-switching, the work done by mechanical stresses has to be taken into account, and the criterion is then

$$\sigma_{ij} \Delta \varepsilon_{ij} + E_i \Delta P_i \geqslant 2P_s E_c, \tag{2}$$

where σ_{ij} and ε_{ij} denote the stress and the strain tensors, respectively. Note that 90°-switching may occur without the presence of external electric fields. Eqs. (1) and (2) represent typically simplified versions of thermodynamic energy-based switching criteria, where the magnitude of polarization is generally assumed to be constant. Furthermore, the inclusion model is often adopted in the development of a polarization-switching criterion, in which the switching criterion is derived from the potential energy of an infinite homogeneous ferroelectric medium containing a single ellipsoidal and transformable inclusion [9].

In general, a domain-switching model requires the development of new constitutive equations and extensive numerical calculations. For example, a nonlinear constitutive model was proposed for ferroelectric polycrystals under a combination of mechanical stress and electric field by employing self-consistent analysis, as an extension of the self-consistent crystal plasticity scheme, to address ferroelectric switching and to estimate the macroscopic response of tetragonal crystals under a variety of loading paths [10]. This model has the ability to capture several observed features of ferroelectrics such as the shapes of the dielectric hysteresis and the butterfly loop, the Bauschinger effect under mechanical and electrical loads, and the depolarization of a polycrystalline by compressive stresses. In numerical simulations of the nonlinear behavior of a ferroelectric polycrystal, the response of the ferroelectric polycrystal to applied loads was predicated by averaging the response of individual grains that were considered to be statistically random in orientation [8]. The nonlinear electric displacement versus electric field hysteresis loops [11] and stress–strain curves [12] were simulated by using a finite element model in which each finite element represented one crystallite and was randomly assigned a crystallographic orientation and a polarization direction. The material responses to the applied electric and/or mechanical fields were averaged over the switching responses of many randomly oriented elements [11,12]. Furthermore, a continuous domain orientation distribution function (ODF) could be used to develop domain-switching models with the consideration of electromechanical interactions in a self-consistent manner and with different constitutive laws to account for strain saturation, asymmetry in tension versus compression, Bauschinger effects, reverse switching and spontaneous strain reorientation [13–17].

It should be noted that most works available on analytical modeling of domain switching are first order approximations, since the related analyses do not take into account the interactions between domains during the switching process. Secondly, many analytical models assume that the switching is the entire response of an "inclusion" and no partial transformation is allowed. In a lot of cases, the electric characteristics, such as the electric boundary conditions between domains, are ignored. In fact, domain switching is a gradual process and crystalline cells in a domain do not all switch simultaneously. The process of domain switching may start with few crystalline cells, i.e., with nominal new domain nucleation and then proceed by domain wall motion. Obviously, the process of domain switching is strictly a kinetic process involving changes in the domain microstructure and a reverse in the macroscopic polarization might be induced by a microscopically complete change in the domain structure. On this aspect, phase-field simulations of the nonlinear behavior of ferroelectrics are able to give insights into the switching mechanism.

Phase-field theory is based on fundamental principles of thermodynamics and kinetics. It provides a powerful method for predicting the temporal evolution of microstructures in materials [18–24]. In a phase-field model, thermodynamic energies are described in terms of a set of continuous order parameters. The temporal evolution of a microstructure is obtained by solving kinetics equations that govern the time-dependence of the spatially inhomogeneous order parameters. A phase-field model does not make any prior assumptions about transient microstructures, which may appear on a phase transformation path, and about transformation criteria. Phase transformation is a direct consequence of the minimization process of the total free energy of an entire simulated system. Phase-field models have been widely used to study domain structures in ferroelectric materials and polarization switching under an electric field [25–37]. For example, Cao and Cross [27] proposed a three-dimensional Landau–Ginzburg model to describe the tetragonal twin microstructure in ferroelectrics. They presented quasi-one-dimensional analytic solutions for the space profiles of the order parameter for 180°- and 90°-twin microstructures. Based on the time-dependent Ginzburg–Landau equation, Nambu and Sagala [28] simulated domain structures in ferroelectrics with consideration of multiple-dipole–dipole–elastic interactions. By taking into account multiple-dipole–dipole–electric and multiple-dipole–dipole–elastic interactions, Hu and Chen [30,31] conducted the two- and three-dimensional phase-field simulations of ferroelectric domain structures and found that the multiple-dipole–dipole–elastic interactions played a critical role in the formation of the twin microstructure, whereas the multiple-dipole–dipole–electric interactions were responsible for the head-to-tail arrangements of the dipoles at twin boundaries. Recently, Li et al. [33–35] extended the phase-field model to study the stability and evolution of domain microstructures in thin films and the effect of electrical boundary conditions as well. Ahluwalia and Cao [36,37] investigated the size dependence of domain patterns and the influence of dipolar defects on the switching behavior of ferroelectrics. However, the polarization switching of ferroelectrics subjected to external electrical and/or mechanical loading has not been comprehensively simulated with the phase-field theory.

In this paper, we conduct phase-field simulations of ferroelectric/ferroelastic polarization switching in a single ferroelectric crystal subjected to external electrical and/or mechanical loading. The phase-field simulations are based on the time-dependent Ginzburg–Landau equation, which takes the multiple-dipole–dipole–elastic and -electric interactions into account. The phase-field model does not make any prior assumptions about the evolution of the domain structure. Polarization switching is a natural process occurring during the minimization of the total free energy of the entire simulated ferroelectric with given boundary and/or loading conditions. With phase-field simulations, we investigate the temporal evolution of polarization under an applied electric field or mechanical stress, the domain configuration, and the macroscopically electrical and mechanical responses to applied electrical and mechanical loads.

2. Simulation methodology

The paraelectric-to-ferroelectric phase transition occurs in a ferroelectric material when its temperature is lower than its Curie point. The spontaneous polarization vector, $\mathbf{P} = (P_1, P_2, P_3)$, is usually used as the order parameter to calculate thermodynamic energies of the ferroelectric phase in the Landau phase transformation theory. As mentioned above, the ferroelectric phase forms a domain structure consisting of domains and domain walls. In most circumstances, domains arrange themselves in a head-to-tail manner. Applying an electric and/or stress field has the tendency to move domain walls or the tendency to nucleate new domains. Polarization switching occurs when the applied electric and/or stress field is high enough to move domain walls and/or to nucleate new domains. In the process of polarization switching, the spontaneous polarization vector, $\mathbf{P}$, changes with time and location such that a new domain configuration is formed with a free energy lower than that of the initial domain configuration. In phase-field simulations, the time-dependent Ginzburg–Landau equation,

$$\frac{\partial P_i(\mathbf{r},t)}{\partial t} = -L\frac{\delta F}{\delta P_i(\mathbf{r},t)} \quad (i = 1,2,3), \tag{3}$$

is generally used to calculate the temporal evolution, where t denotes time, L is the kinetic coefficient, F is the total free energy of the system, $\delta F/\delta P_i(\mathbf{r},t)$ represents the thermodynamic driving force for the spatial and temporal evolution of the simulated system, and $\mathbf{r}$ denotes the spatial vector, $\mathbf{r} = (x_1, x_2, x_3)$. In the present study, we adopt Eq. (3) to simulate the spontaneous polarization and the process of polarization switching in a ferroelectric under an applied electrical or mechanical field. The total free energy of the system includes the bulk free energy, the domain wall energy, i.e., the energy of the spontaneous polarization gradient, the multiple-dipole–dipole–electric and multiple-dipole–dipole–elastic interaction energies, and the elastic energy and the electric energy induced by an applied electrical or mechanical load.

For a ferroelectric material, the bulk Landau free energy density is commonly expressed by a six-order polynomial of the spontaneous polarization [31], i.e.,

$$\begin{aligned} f_{\mathrm{L}} = {} & \alpha_1(P_1^2 + P_2^2 + P_3^2) + \alpha_{11}(P_1^4 + P_2^4 + P_3^4) \\ & + \alpha_{12}(P_1^2P_2^2 + P_2^2P_3^2 + P_1^2P_3^2) + \alpha_{111}(P_1^6 + P_2^6 + P_3^6) \\ & + \alpha_{112}[P_1^4(P_2^2 + P_3^2) + P_2^4(P_1^2 + P_3^2) + P_3^4(P_1^2 + P_2^2)] \\ & + \alpha_{123}P_1^2P_2^2P_3^2, \end{aligned} \tag{4}$$

where $\alpha_{11}, \alpha_{12}, \alpha_{111}, \alpha_{112}, \alpha_{123}$ are constant coefficients and $\alpha_1 = (T - T_0)/2\varepsilon_0 C_0 = 1/2\varepsilon$ is linked to the dielectric constant, ε, for $T > T_0$, T and T_0 denote temperature and the Curie–Weiss temperature, respectively, C_0 is the Curie constant, and ε_0 is the dielectric constant of vacuum.

In the Ginzburg–Landau theory, the free energy function also depends on the gradient of the order parameter. For ferroelectric materials, the polarization gradient energy represents the domain wall energy. For simplicity, the lowest order of the gradient energy density is used here, which takes the form [31]:

$$\begin{aligned} f_{\mathrm{G}}(P_{i,j}) = {} & \frac{1}{2}G_{11}(P_{1,1}^2+P_{2,2}^2+P_{3,3}^2) \\ & + G_{12}(P_{1,1}P_{2,2}+P_{2,2}P_{3,3}+P_{1,1}P_{3,3}) \\ & + \frac{1}{2}G_{44}[(P_{1,2}+P_{2,1})^2+(P_{2,3}+P_{3,2})^2+(P_{1,3}+P_{3,1})^2] \\ & + \frac{1}{2}G'_{44}[(P_{1,2}-P_{2,1})^2+(P_{2,3}-P_{3,2})^2+(P_{1,3}-P_{3,1})^2], \end{aligned} \tag{5}$$

where G_{11}, G_{12}, G_{44}, and G'_{44} are gradient energy coefficients and $P_{i,j}$ denotes the derivative of the ith component of the polarization vector, P_i, with respect to the jth coordinate and $i, j = 1, 2, 3$.

In the present phase-field simulations, each element is represented by an electric dipole with its strength of the dipole being given by a local polarization vector. The electric field produced by all dipoles forms an internal electric field, which, in turn, exerts a force on each of the dipoles. The multiple-dipole–dipole–electric interactions play a crucial role in the formation of a head-to-tail domain structure and in the process of domain switching as well. The multiple-dipole–dipole–electric interaction energy density is calculated from [31]

$$f_{\mathrm{dip}} = -\frac{1}{2}\mathbf{E}_{\mathrm{dip}}^{(i)} \cdot \mathbf{P}^{(i)}, \tag{6}$$

where

$$\mathbf{E}_{\mathrm{dip}}^{(i)} = -\frac{1}{4\pi\varepsilon}\int \left\{ \frac{\mathbf{P}(\mathbf{r}_j)}{|\mathbf{r}_i-\mathbf{r}_j|^3} - \frac{3[(\mathbf{r}_i-\mathbf{r}_j)][\mathbf{P}(\mathbf{r}_j)\cdot(\mathbf{r}_i-\mathbf{r}_j)]}{|\mathbf{r}_i-\mathbf{r}_j|^5} \right\} \mathrm{d}^3\mathbf{r}_j \tag{7}$$

is the electric field at point $\mathbf{r}_i$ induced by all dipoles including the image electric field produced by dipole $\mathbf{P}(\mathbf{r}_i)$ itself. When there is an externally applied electric field, E_i^{e}, an additional electrical energy density,

$$f_{\mathrm{elec}} = -E_i^{\mathrm{e}} P_i \tag{8}$$

should be taken into account in the simulations.

As mentioned above, spontaneous strains are associated with spontaneous polarizations. The spontaneous eigenstrains are linked to the spontaneous polarization components in the following form,

$$\begin{aligned} \varepsilon_{11}^0 &= Q_{11}P_1^2 + Q_{12}(P_2^2+P_3^2), \\ \varepsilon_{22}^0 &= Q_{11}P_2^2 + Q_{12}(P_3^2+P_1^2), \\ \varepsilon_{33}^0 &= Q_{11}P_3^2 + Q_{12}(P_1^2+P_2^2), \\ \varepsilon_{23}^0 &= Q_{44}P_2P_3, \\ \varepsilon_{13}^0 &= Q_{44}P_1P_3, \\ \varepsilon_{12}^0 &= Q_{44}P_1P_2, \end{aligned} \tag{9}$$

where Q_{ij} are the electrostrictive coefficients. When a dipole is among other dipoles with different orientations, there exist multiple-dipole–dipole–elastic interactions. The multiple-dipole–dipole–elastic interactions play an essential role in the determination of a domain structure. A twin-like domain structure is formed when the multiple-dipole–dipole–elastic interactions predominate [30]. It is still a challenging task to calculate the multiple-dipole–dipole–elastic interaction energy for arbitrary boundary conditions. However, with periodic boundary conditions, which are adopted in this study, the general solution of the elastic displacement field is given in Fourier space by [38,39]

$$u_i(\boldsymbol{\xi}) = X_j N_{ij}(\boldsymbol{\xi})/D(\boldsymbol{\xi}), \tag{10}$$

where $X_i = -\mathrm{i}C_{ijkl}\varepsilon_{kl}^0\xi_j$, $\mathrm{i} = \sqrt{-1}$, $N_{ij}(\boldsymbol{\xi})$ are cofactors of a 3×3 matrix $\mathbf{K}(\boldsymbol{\xi})$,

$$\mathbf{K}(\boldsymbol{\xi}) = \begin{bmatrix} K_{11} & K_{12} & K_{13} \\ K_{21} & K_{22} & K_{23} \\ K_{31} & K_{32} & K_{33} \end{bmatrix}, \tag{11}$$

and $D(\boldsymbol{\xi})$ is the determinant of matrix $\mathbf{K}(\boldsymbol{\xi})$. Note that $K_{ki}(\boldsymbol{\xi}) = C_{kjil}\xi_j\xi_l$, in which C_{ijkl} and ξ_i are the elastic constant components and coordinates in Fourier space, respectively.

In the present simulations, we consider a ferroelectric material, which has a perovskite crystal structure and its lattice changes from cubic to tetragonal when spontaneous polarization occurs. In this case, the cubic paraelectric phase serves as the background material such that all electric dipoles are embedded within the background material. For cubic crystals, the explicit expressions of $D(\boldsymbol{\xi})$ and $N_{ij}(\boldsymbol{\xi})$ are

$$\begin{aligned} D(\xi) &= \mu^2(\lambda+2\mu+\mu')\xi^6 + \mu'(2\lambda+2\mu+\mu') \\ &\quad \times \xi^2(\xi_1^2\xi_2^2+\xi_2^2\xi_3^2+\xi_1^2\xi_3^2) \\ &\quad + \mu'^2(3\lambda+3\mu+\mu')\xi_1^2\xi_2^2\xi_3^2, \\ N_{11}(\xi) &= \mu^2\xi^4 + \beta\xi^2(\xi_2^2+\xi_3^2) + \gamma\xi_2^2\xi_3^2, \\ N_{12} &= -(\lambda+\mu)\xi_1\xi_2(\mu\xi^2+\mu'\xi_3^2), \end{aligned} \tag{12}$$

and the other components are obtained by the cyclical permutation of 1, 2, 3, where

$$\begin{aligned} & \xi^2 = \xi_i\xi_i, \quad \beta = \mu(\lambda+\mu+\mu'), \\ & \gamma = \mu'(2\lambda+2\mu+\mu'), \quad \lambda = c_{12}, \quad \mu = c_{44}, \\ & \quad \text{and} \quad \mu' = c_{11} - c_{12} - 2c_{44}. \end{aligned} \tag{13}$$

Polarization and/or polarization switching change the dimensions and/or orientations of each crystalline cell in the solid and thus produce local displacements, $u_i^{(\mathrm{s})}$, $i = 1, 2, 3$, and strains. We may call these the polarization-related displacements and strains and they are linked by the equation:

$$\varepsilon_{ij}^{(\mathrm{s})} = \frac{1}{2}\left(u_{i,j}^{(\mathrm{s})} + u_{j,i}^{(\mathrm{s})}\right). \tag{14}$$

Due to the constraint of the surroundings, the polarization-related strains include two parts: the elastic strains and the eigenstrains. The elastic strains related to polarization and/or polarization switching are given by

$$e_{ij}^{\mathrm{ela,s}} = \varepsilon_{ij}^{(\mathrm{s})} - \varepsilon_{ij}^{0}. \tag{15}$$

When there exists an externally applied homogeneous stress, σ_{kl}^{e}, using the superposition principle, we have the total elastic strains of the system:

$$\varepsilon_{ij}^{\mathrm{ela}} = \varepsilon_{ij}^{(\mathrm{s})} - \varepsilon_{ij}^{0} + S_{ijkl}\sigma_{kl}^{\mathrm{e}}, \tag{16}$$

where S_{ijkl} is the elastic compliance matrix of the background material. Finally, the elastic strain energy density under the cubic approximation is given by

$$\begin{aligned} f_{\mathrm{E}} = & \frac{1}{2}c_{11}[(\varepsilon_{11}^{\mathrm{ela}})^2 + (\varepsilon_{22}^{\mathrm{ela}})^2 + (\varepsilon_{33}^{\mathrm{ela}})^2] \\ & + c_{12}[\varepsilon_{11}^{\mathrm{ela}}\varepsilon_{22}^{\mathrm{ela}} + \varepsilon_{22}^{\mathrm{ela}}\varepsilon_{33}^{\mathrm{ela}} + \varepsilon_{11}^{\mathrm{ela}}\varepsilon_{33}^{\mathrm{ela}}] \\ & + 2c_{44}[(\varepsilon_{12}^{\mathrm{ela}})^2 + (\varepsilon_{23}^{\mathrm{ela}})^2 + (\varepsilon_{13}^{\mathrm{ela}})^2]. \end{aligned} \tag{17}$$

As described above, the elastic strain energy density is a function of polarization and applied stresses. An applied electric field can change the polarization and consequently vary the elastic strain energy density. On the other hand, an applied stress field can also change the polarization and thus change the electric energy density.

Integrating the free energy density over the entire volume of a simulated ferroelectric yields the total fee energy, F, of the simulated ferroelectric under externally applied electrical and mechanical loads, E_i^{e} and σ_{kl}^{e}. Mathematically, we have

$$F = \int_V \left[f_{\mathrm{L}}(P_i) + f_{\mathrm{G}}(P_{i,j}) + f_{\mathrm{dip}}(P_i) + f_{\mathrm{elec}}(P_i, E_i^{\mathrm{e}}) + f_{\mathrm{E}}(P_i, \sigma_{kl}^{\mathrm{e}}) \right] \mathrm{d}V, \tag{18}$$

where V is the volume of the simulated ferroelectric.

For convenience of simulations, we employ the following set of the dimensionless variables as used in the literature [31]

$$\begin{aligned} & \mathbf{r}^* = \sqrt{|\alpha_1|/G_{110}}\mathbf{r}, \quad t^* = |\alpha_1|Lt, \quad \mathbf{P}^* = \mathbf{P}/P_0, \\ & \alpha_1^* = \alpha_1/|\alpha_1|, \quad \alpha_{11}^* = \alpha_{11}P_0^2/|\alpha_1|, \quad \alpha_{12}^* = \alpha_{12}P_0^2/|\alpha_1|, \\ & \varepsilon^* = 1/(2|\alpha_1^*|), \\ & \alpha_{111}^* = \alpha_{11}P_0^4/|\alpha_1|, \quad \alpha_{112}^* = \alpha_{112}P_0^4/|\alpha_1|, \\ & \alpha_{123}^* = \alpha_{123}P_0^4/|\alpha_1|, \\ & Q_{11}^* = Q_{11}P_0^2, \quad Q_{12}^* = Q_{12}P_0^2, \quad Q_{44}^* = Q_{44}P_0^2, \\ & E^{\mathrm{e},*} = E^{\mathrm{e}}/(|\alpha_1|P_0), \quad \sigma_{kl}^{\mathrm{e},*} = \sigma_{kl}^{\mathrm{e}}/(|\alpha_1|P_0^2), \\ & c_{11}^* = c_{11}/(|\alpha_1/P_0^2), \quad c_{12}^* = c_{12}/(|\alpha_1|P_0^2), \\ & c_{44}^* = c_{44}/(|\alpha_1|P_0^2), \\ & G_{11}^* = G_{11}/G_{110}, \quad G_{12}^* = G_{12}/G_{110}, \\ & G_{44}^* = G_{44}/G_{110}, \quad G_{44}'^* = G_{44}'/G_{110}, \end{aligned} \tag{19}$$

where $P_0 = |\mathbf{P}_0| = 0.757\ \mathrm{C/m^2}$ is the magnitude of the spontaneous polarization at room temperature, $\alpha_1 = (T - T_0)/(2\varepsilon_0 C_0) = (25 - 479)3.8 \times 10^5\ \mathrm{m^2N/C^2}$, and $G_{110} = 1.73 \times 10^{-10}\ \mathrm{m^4N/C^2}$ is a reference value of the gradient energy coefficients [34]. The values of the dimensionless (normalized) material coefficients used in the simulations are listed in Table 1.

With the dimensionless variables and Eq. (18), we rewrite the time-dependent Ginzburg–Landau equation

$$\begin{aligned} & \frac{\partial P_i^*(\mathbf{r}^*, t^*)}{\partial t^*} \\ & = -\frac{\delta \int \left[f_{\mathrm{L}}\left(P_i^*\right) + f_{\mathrm{dip}}(P_i^*) + f_{\mathrm{elec}}(P_i^*, E_i^{\mathrm{e},*}) + f_{\mathrm{E}}(P_i^*, \sigma_{kl}^{\mathrm{e},*}) \right] \mathrm{d}V^*}{\delta P_i^*} \\ & \quad - \frac{\delta \int f_{\mathrm{G}}\left(P_{i,j}^*\right) \mathrm{d}V^*}{\delta P_i^*}. \end{aligned} \tag{20}$$

In Fourier space, Eq. (20) takes the form [31]

$$\frac{\partial}{\partial t^*}\hat{P}_i(\boldsymbol{\xi}, t^*) = -\{\hat{f}(P_i^*)\}_{\boldsymbol{\xi}} - G_i\hat{P}_i(\boldsymbol{\xi}, t^*), \tag{21}$$

where $\hat{P}_i(\boldsymbol{\xi}, t^*)$ and $\{\hat{f}(P_i^*)\}_{\boldsymbol{\xi}}$ are the Fourier transformations of $P_i^*(\mathbf{r}^*, t^*)$ and

$$\frac{\delta \int [f_{\mathrm{L}}(P_i^*) + f_{\mathrm{dip}}(P_i^*) + f_{\mathrm{elec}}(P_i^*, E_i^{\mathrm{e},*}) + f_{\mathrm{E}}(P_i^*, \sigma_{kl}^{\mathrm{e},*})] \mathrm{d}V^*}{\delta P_i^*},$$

respectively. G_is are the gradient operators corresponding to the ith-component of the polarization field, which are defined as follows:

$$\begin{aligned} G_1 &= G_{11}^*\xi_1^2 + (G_{44}^* + G_{44}'^*)(\xi_2^2 + \xi_3^2), \\ G_2 &= G_{11}^*\xi_2^2 + (G_{44}^* + G_{44}'^*)(\xi_1^2 + \xi_3^2), \\ G_3 &= G_{11}^*\xi_3^2 + (G_{44}^* + G_{44}'^*)(\xi_2^2 + \xi_1^2). \end{aligned} \tag{22}$$

The semi-implicit Fourier-spectral method [31] was employed to solve the partial differential equation (21) in the present work.

3. Simulation results and discussion

The methodology described in Section 2 is for three-dimensional simulations. In the present study, we conducted two-dimensional (2D) simulations of polarization and polarization switching under the plane-strain condition. In the 2D simulations, electric charges and dipoles should be regarded as line charges and dipoles and the pre-factor, $1/(4\pi\varepsilon)$, in Eq. (7) should be changed to $1/(2\pi\varepsilon)$. In the simulations, we used 32×32 discrete grid points with a cell size of $\Delta x^* = \Delta y^* = 1$ and adopted periodic boundary conditions in both the x and y

Table 1
Values of the normalized coefficients used in the simulation [34]

α_1^*	α_{11}^*	α_{12}^*	α_{111}^*	α_{112}^*	α_{123}^*	Q_{11}^*	Q_{12}^*	Q_{44}^*	c_{11}^*	c_{12}^*	c_{44}^*	G_{11}^*	G_{12}^*	G_{44}^*	$G_{44}'^*$
−1	−0.24	2.5	0.49	1.2	−7	0.05	−0.015	0.019	1766	802	1124	1.60	0.0	0.8	0.8

directions. The periodic boundary conditions imply that the simulated domain structure reflects a domain structure within an infinitely large single crystal, in which there are no free edges and thus the edge effect is not considered. In 2D phase-field simulations, a domain structure is represented by a polarization field, which varies spatially and, at each lattice site, is characterized by a two-component vector. To visualize the simulation results, we denote the magnitude and direction of each polarization vector by the length and direction of an arrow in the plots. In the numerical calculations of Eq. (21), the time step was set at $\Delta t^* = 0.04$.

3.1. Formation of a ferroelectric domain structure

Fig. 1 shows the temporal evolution of a domain structure without applied electrical and mechanical loading, but with the mechanical clamped boundary conditions, which mean that the dimensions of the simulated region are fixed. At the beginning of the evolution, a Gaussian random fluctuation was introduced to initiate the polarization evolution process. After 40 steps, the polarization is still in the nucleation state, as shown Fig. 1(a), in which the arrows at the center grid points are longer than those in the other regions and align along a direction, thereby looking like a domain nuclei. Fig. 1(b) illustrates the polarization distribution after 80 steps of evolution, indicating that the domain at the center grows. 90°-domain walls appear after 120 steps of evolution, as shown in Fig. 1(c). Figs. 1(d) and (e) demonstrate the temporal structures after 240 and 500 steps of evolution, respectively, showing that the magnitude of the maximum polarization does not increase any more, but the domain structure changes by domain wall motion. It is interesting to note that there is a 180°-domain wall between the left corner domain and the center domain in Fig. 1(d) or (e), at which the polarizations change the magnitude to form the head-to-head 180°-domain wall with almost zero magnitude of polarizations at the middle of the wall. The domain at the left bottom corner in Fig. 1(d) or (e) shrinks, as the evolution proceeds, and the other three domains continue to grow, finally forming a twin structure after 1000 steps of evolution, as shown in Fig. 1(f). A twin-like domain structure indicates that the strain energy predominates in the simulated system. After 1000 steps of evolution, the domain structure becomes steady and no longer changes with time. At the steady state, the dipoles at the twin boundaries all have head-to-tail arrangements, which is consistent with a previous study [30]. It should be pointed out that a nonzero value of the average polarization over the entire simulated region exists in the steady domain structure and associated with the nonzero average polarization is an internal stress field in the simulated region with nonzero average stresses, which are induced by the fixed dimensions. Nevertheless, when the spontaneous domain structure is available, we are able to simulate polarization switching of the domain structure under external electrical or mechanical loading.

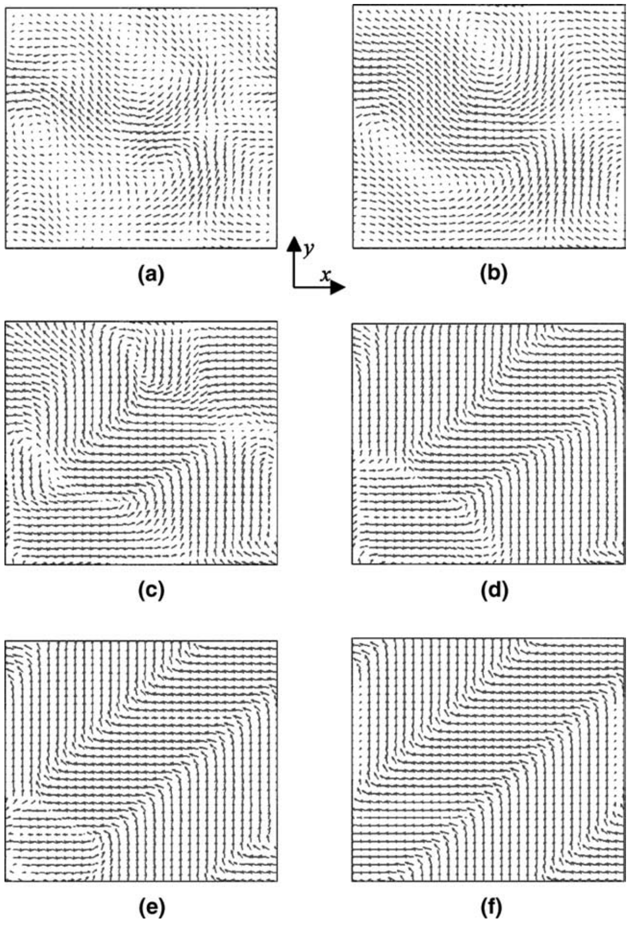

Fig. 1. Temporal evolution of domain structure formation in a two-dimensional model: (a) 40 steps; (b) 80 steps; (c) 120 steps; (d) 240 steps; (e) 500 steps and (f) 1000 steps.

3.2. Polarization switching subjected to an applied electric field

Figs. 2(a)–(f) show the temporal evolution of polarization switching when an external electric field with a dimensionless strength of $E_x^{e,*} = 0.5$ is applied along the positive x-direction to the initial domain structure illustrated in Fig. 2(a), which is a copy of Fig. 1(f). Again, the periodic boundary conditions are adopted here with the fixed dimensions of the simulated region. Comparing Fig. 2(a) and (b) indicates that the applied electric field drives the domain walls to move at the early stage of switching. The motion of the domain walls causes the domains with the original polarization parallel to the positive y-direction to grow and the other domains to shrink. More important and significant than the domain wall motion is that the dipoles in the two growing

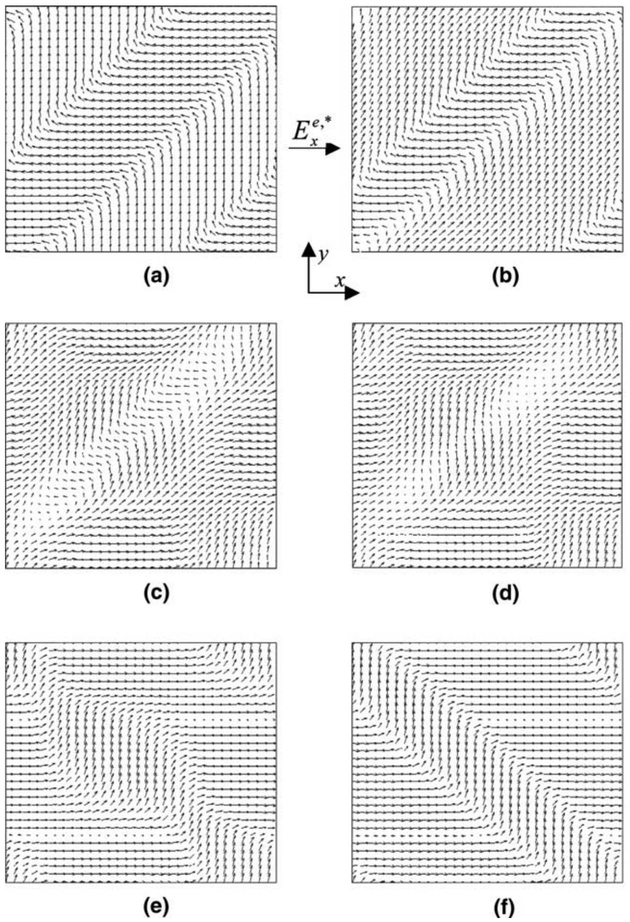

Fig. 2. Temporal evolution of polarization switching under an externally applied electric field of $E_x^{e,*}$: (a) initial state; (b) 70 steps; (c) 100 steps; (d) 110 steps; (e) 140 steps and (f) 200 steps.

domains rotate their polarization directions clockwise ununiformly by certain degrees, trying to align themselves with the applied field, as seen in Fig. 2(b), and meanwhile the domain walls also become wider. After 100 and 110 evolution steps, the initial domain structure fades away and new domains, in which dipoles have aligned themselves completely with the applied field, begin to nucleate symmetrically about the original domain wall, as seen in Figs. 2(c) and (d). The newly formed domains are then expanded through the motion and change of the newly formed, curved and irregular domain walls. Fig. 2(e) shows that the new domains gradually become large, but the domain walls are still not straight after 140 steps of evolution. Finally, the new domain structure reaches a steady state after 200 steps of evolution. At the steady state, all domain walls are straight again and no longer move under the external electric field, as shown in Fig. 2(f). By comparing Fig. 2(f) and (a), one can see that the applied electric field changes the average polarization in the x-direction, P_x^*, from negative in the initial state, as shown in Fig. 2(a), to positive in the final state, as shown Fig. 2(f), thereby revising the average polarization, P_x^*. In addition to the alignment of the average polarization along the direction of the applied electric field, the applied field increases the magnitude of P_x^* from -0.3463 to 0.5311, thereby indicating that some dipoles with initial polarizations along the y-direction switch their polarizations by 90°. Actually, from Figs. 2(a)–(f), one can find that some dipoles rotate by 90°, some rotate by 180°, and some remain unchanged. The results indicate that the external electric field can simultaneously induce both 90°-and 180°-polarization switching and the polarization switching is not constrained within certain original domains. The ratio of the polarization along the y-axis to the polarization along the x-axis changes from about -1.185 at the initial state to about 0.4824 at the final steady state. The temporal evolution results indicate that the macroscopic reversal of the average polarization, P_x^*, does not simply imply a microscopic 180°-switch of the domains originally having a polarization along the x-direction. The minimization of the free energy of the entire system under the external electric field changes the domain structure completely. The temporal evolution of polarization switching in Figs. 2(a)–(f) also shows that the domain switching is a kinetic process of the disappearance of old domains and the nucleation and growth of new domains, in which the new domain growth is accomplished mainly through domain wall motion. Not only are the directions of the domains after switching different from those of the initial domains, but the domain size and configuration are also different. The domain structure is completely changed after the switch.

3.3. Polarization switching subjected to an external stress

We simulated polarization switching induced by an applied compressive stress along the y-direction with a dimensionless level of $\sigma_{yy}^{e,*} = -14$, which corresponded a strain field, $\varepsilon_{ij}^{e} = S_{ijkl}\sigma_{kl}^{e}$. The stress was applied prior to the evolution and the periodic boundary conditions were again adopted in the evolution calculations with the fixed dimensions. Since the evolution was calculated at the fixed dimensions, stresses changed during the evolution but the applied strains remained unchanged. Exactly speaking, we simulated polarization switching subjected to an external strain field. Figs. 3(a)–(f) show the temporal evolution of polarization switching, in which Fig. 3(a) copied from Fig. 1(f) shows the initial domain configuration. Since the energy-favorite domains exist in the initial domain structure, no domain nucleation is needed in the polarization switching. The polarization switching is accomplished by domain wall motion. As a result of the domain wall motion, the domains with original orientations parallel to the y-axis shrink, whereas the domains with original orientations perpendicular to the y-axis grow, as shown in Figs. 3(b)–(d).

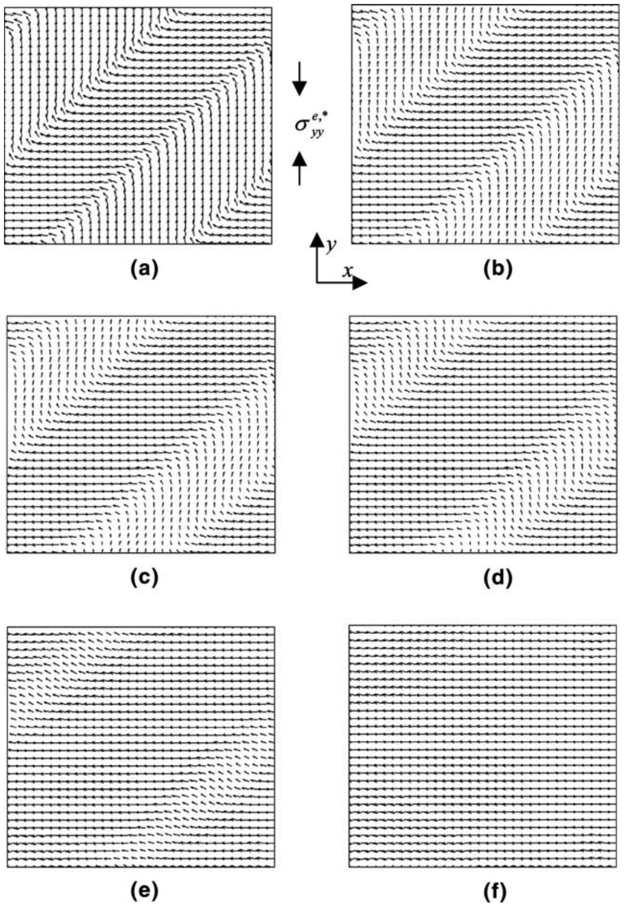

Fig. 3. Temporal evolution of polarization switching subjected to an external compressive stress of $\sigma_{yy}^{e,*} = -14$: (a) initial state; (b) 15 steps; (c) 25 steps; (d) 45 steps; (e) 105 steps and (f) 200 steps.

Fig. 3(e) illustrates the temporal configuration of the domain structure after 105 steps of evolution, showing a wide transition region. The wide transition region is formed at a temporal state, at which the original domain wall between the domains with initial polarizations parallel to the x- and y-direction merges with the next original domain wall between the domains with initial polarizations parallel to the y- and x-direction, and the original domains with initial polarizations parallel to the y-direction disappear. After 200 steps of evolution, the entire region becomes a single domain with all dipoles parallel to the x-axis, as seen in Fig. 3(f). Li et al. [40] investigated the process of 90°-domain switching in tetragonal $BaTiO_3$ and $PbTiO_3$ single crystals under external stresses. Our simulation results agree with their experimental observations that single-domain crystals can be obtained from polydomain-structured specimens by the application of a compressive stress. The single-domain structure is steady under the compressive stress and does not change with time any more. Comparing the final state to the initial state of the domain structure, as shown in Figs. 3(a) and (f), indicates that only 90°-polarization switching occurs under the externally applied stress. The 90°-polarization switching changes the strain distribution, lowers the strain energy, and then minimizes the free energy of the entire system. There is no 180°-polarization switching under the stress load because the 180°-polarization switching does not change the strain energy in the materials. The results are consistent with the predictions from the continuum theory that mechanical loading can cause only 90°-polarization switching in ferroelectric materials.

3.4. Polarization versus electric field and strain versus electric field

It is polarization switching that causes ferroelectric materials to exhibit nonlinear electrical and mechanical behaviors. In order to characterize the nonlinear behaviors of ferroelectric materials, we simulated the polarization and strain responses at different levels of external electric loading with the periodic boundary conditions and the fixed dimensions of the simulated region. The external electric field was applied prior to the evolution calculations along the y-axis, where a positive or negative electric field meant that the field was parallel or anti-parallel to the y-direction. In the simulations, the applied dimensionless field increased from 0 to 0.5, then decreased from 0.5 to −0.6, and then increased from −0.6 to 0.5 at the same increment or decrement amount of 0.05 in the dimensionless electric field strength. At each level of electric field loading, we calculated the evolution of the domain structure in the same way as described above, but only the final state of polarization distribution was considered to be the corresponding response of the simulated system under such a level of electric loading. At the time step of $\Delta t^* = 0.04$, 2000 steps of evolution conducted at each level of the applied electric field were sufficient to ensure that the domain structure reached a steady state. At each final steady state, the average polarization and the average strain along the y-direction were taken as the macroscopic response of the simulated ferroelectric to the applied electric field. As mentioned above, the simulations were conducted at fixed dimensions. Thus, macroscopically average strains should remain zero or predescribed values during the evolution calculations. However, fixed dimensions cause macroscopically average stresses to change during domain structure evolution. To present the simulation results in a conventional manner, we convert macroscopically average stresses to macroscopically average strains via Hooke's law. Without any applied mechanical loads, from Eq. (16) and Hooke's law, we have the stresses, $\sigma_{kl}^{(s)}$, linked to polarizations

$$\sigma_{kl}^{(s)} = c_{klij}\varepsilon_{ij}^{\mathrm{ela,s}} = c_{klij}\left(\varepsilon_{ij}^{(s)} - \varepsilon_{ij}^{0}\right). \tag{23}$$

Since we fixed the dimensions in the simulations, the average strains, $\langle \varepsilon_{ij}^{(s)} \rangle$, were all zero. The average strains, $\langle \varepsilon_{ij}^{0} \rangle$, were then determined from the average stresses, $\langle \sigma_{kl}^{(s)} \rangle$,

$$\left\langle \varepsilon_{ij}^{0} \right\rangle = -S_{ijkl} \left\langle \sigma_{kl}^{(s)} \right\rangle. \tag{24}$$

Eq. (24) indicates that the average strains, $\langle \varepsilon_{ij}^{0} \rangle$, represent the average stresses $\langle \sigma_{kl}^{(s)} \rangle$ induced by domain structure evolution under the condition of fixed dimensions. We may image that after the evolution, the average strains, $\langle \varepsilon_{ij}^{0} \rangle$, will be produced if we release the average stresses $\langle \sigma_{kl}^{(s)} \rangle$. Note that domain structure evolution under the condition of fixed dimensions could be completely different from that under fixed average stresses. For simplicity, we shall not discuss the difference further.

In the present study, we use the average strain, $\langle \varepsilon_{yy}^{0} \rangle$, to represent the relative change in the dimension of a ferroelectric along the y-direction, i.e., along the applied field direction. The average strain, $\langle \varepsilon_{yy}^{0} \rangle$, could be obtained by using Eq. (9) to calculate the value of ε_{yy}^{0} at each point on the grid and then averaging ε_{yy}^{0} over the simulated region. Alternately, the average strain, $\langle \varepsilon_{yy}^{0} \rangle$, could be obtained from the average stresses, $\langle \sigma_{kl}^{(s)} \rangle$, which were calculated by taking the average of the polarization-linked stresses, $\sigma_{kl}^{(s)}$, at each point on the grid. Due to the nonlinear behavior, the response of a ferroelectric material to an applied load depends on the loading history. Therefore, the final state of the domain structure under a given level of loading was taken as the initial state for the next level of loading in the simulations. The final state of the spontaneous polarization shown in Fig. 1(f) was used as the starting state of the domain structure. As mentioned above, the initial residual average polarization and the initial residual average strain have finite values, which are 0.325 and 0.535%, respectively, and shown by point O in Figs. 4 and 5.

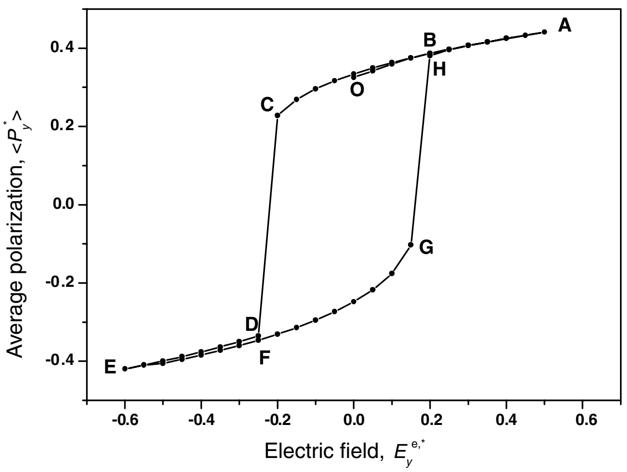

Fig. 4. A simulated hysteresis loop of average polarization versus applied electric field.

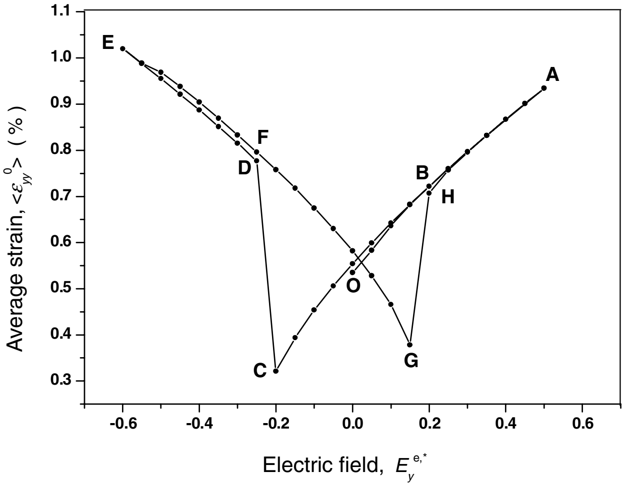

Fig. 5. A simulated butterfly loop of strain versus electric field.

Fig. 4 shows simulated results of the average polarization versus the electric field, while Fig. 5 illustrates simulated results of the average strain versus the electric field. The domain structures corresponding to points O and A–H on the graphs in Figs. 4 and 5 are shown in Figs. 2(f) and 6(a)–(h). From the starting point, O, applying a positive electric field increases the average polarization, $\langle P_y^{*} \rangle$, and the average strain, $\langle \varepsilon_{yy}^{0} \rangle$, as shown in Figs. 4 and 5. At the applied electric field of 0.5, the average polarization, $\langle P_y^{*} \rangle$, and the average strain, $\langle \varepsilon_{yy}^{0} \rangle$, reach 0.441 and 0.934%, respectively, as marked by A in Figs. 4 and 5, and the corresponding domain structure is shown in Fig. 6(a). Comparing Fig. 6(a) with Fig. 1(f) indicates that the domains having polarizations along the positive y-direction grow, whereas the domains having polarizations along the x-direction shrink. Since energy-favorite domains exist, no domain nucleation occurs and the change in the domain structure is accomplished by domain wall motion. At point A, however, the simulated region still contains many domains, indicating that the domain structure has not reached a saturated state with only a single domain. During the decrease of the applied electric field from A to B and to zero, the average polarization and the average strain decrease smoothly, as shown in Figs. 4 and 5, respectively, which is attributed to the smooth domain wall motion, as indicated by the domain structures illustrated in Figs. 6(a) and (b). Note that domain wall motion means partial domain switching, i.e., the regions swept by the domain walls are switched. When the applied electric returns to zero, the residual average polarization and the residual average strain are slightly higher than the corresponding original values, as shown Figs. 4 and 5. Then, the applied electric field changes its sign to negative. The smooth changes in the average polarization and the average strain with the

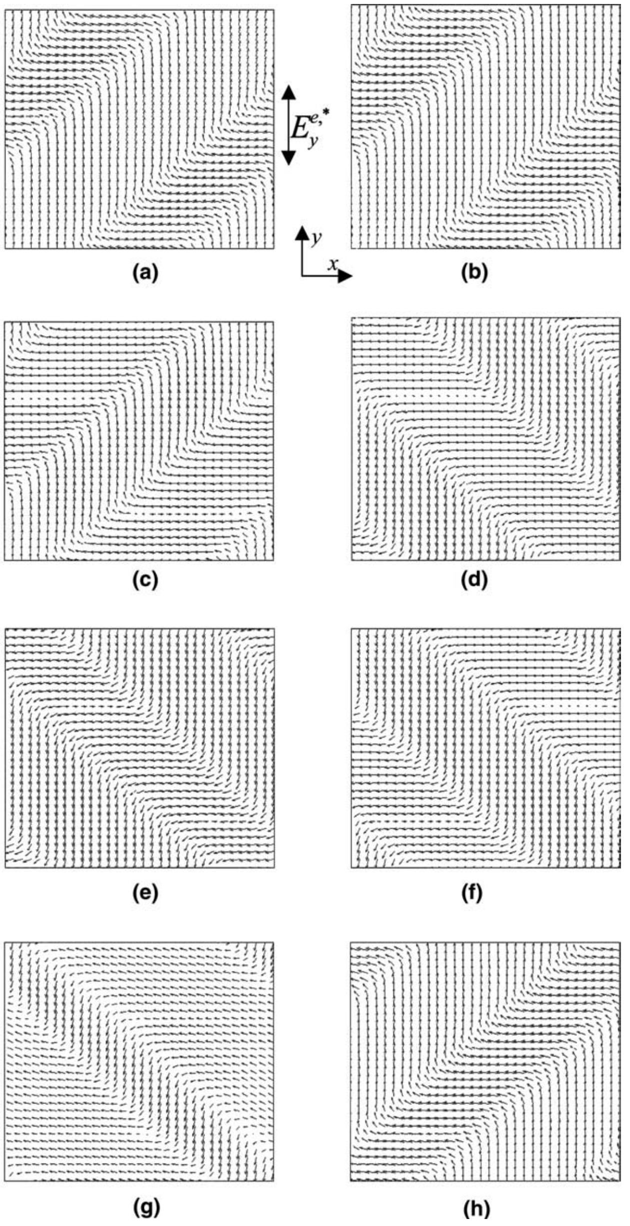

Fig. 6. Domain structures corresponding to points A–H in Figs. 4 and 5.

applied field continue until point C marked in Figs. 4 and 5, at which jumps occur. The jump in the average polarization reverses the direction of the average polarization, whereas the jump in the average strain does not change the sign of the average strain because the average strain is calculated by taking the paraelectric phase as the stress-free or strain-free state. As expected, the jumps are attributed to a great change in the domain structure, which is demonstrated in Figs. 6(c) and (d), showing that the dipoles parallel to the *y*-axis all change their directions. Macroscopically, the absolute strength of the applied electric field reversing the average polarization direction is called the coercive field, which is 0.2 in the dimensionless units for the simulated ferroelectric. At the coercive field, the domain structure changes its configuration completely. As demonstrated in Section 3.2, the complete change in the domain structure is accomplished by nucleation and growth of new domains because there are no energy-favorite domains in the old domain structure. One of the advantages of the phase-field model in predicting ferroelectric nonlinear behavior is that it does not need a domain-switching criterion and the reverse in the average polarization occurs automatically. Comparing Fig. 6(c) and (d) indicates also that some dipoles with polarizations parallel to the negative *x*-direction remain unchanged during the complete change in the domain structure. Further increasing the negative field strength from the coercive field to −0.6 increases the absolute value of the negative average polarization to −0.419 and the amount of the average strain to 1.02%, indicated by point E marked in Figs. 4 and 5. Next, decreasing the applied negative field from −0.6 to −0.25 and then to 0 increases the average polarization from −0.419 to −0.346 and then to −0.248, and decreases the average strain from 1.02% to 0.796% and then to 0.582%. The residual negative average polarization of −0.248 has a lower magnitude than the residual positive average polarization of 0.334 and the residual average strain, 0.582%, yielded from lowering the negative applied electric field is slightly higher than that, 0.554%, resulting from lowering the positive applied electric field. After the zero field, the applied field changes to positive again. Then, the average polarization and the average strain increase smoothly with the applied field until occurrence of jumps, as marked by point G in Figs. 4 and 5. As mentioned above, the smooth changes in the average polarization and the average strain are mainly accomplished by smooth motion of domain walls, i.e., by partial domain switching. When the electric field reaches the coercive field, the average polarization jumps from negative to positive, while the average strain jumps also, as indicated by points G and H in Figs. 4 and 5. Figs. 6(g) and (h) illustrate the domain structures before and after the jumps. As expected, the domain structure changes its configuration completely. It is clearly shown in Figs. 4 and 5 that the coercive field at point G, 0.15, is slightly lower than that, 0.2, at point C, the absolute value of the average polarization at point G, −0.103, is lower than that, 0.228, at point C, and the average strain, 0.378%, at point G is higher than that, 0.321%, at point C, thereby indicating again the asymmetric behavior of the simulated system. The asymmetric behavior of the simulated system might be attributed to the insufficient number of domains used in the present study and/or other reasons. Nevertheless, point H almost coincides with point B in Figs. 4 and 5 and, as expected, the domain structures shown in Figs. 6(b) and (h) are almost identical if one keeps periodic patterns in mind. At this state, the simulated hysteresis loop of average polarization versus the applied electric field and the simulated butterfly loop of average strain versus the applied electric field are completed. After that, further changes in the applied electric field within the range from −0.6 to 0.5 repeat the curves shown in Figs. 4 and 5.

3.5. Stress versus strain

3.5.1. Loading-rate-independent behaviors

In Section 3.3, we report the temporal evolution of the domain structure under an applied compressive stress. In this section, we report the average strain response of the simulated ferroelectric to applied compressive stresses. A uniform stress with its magnitude ranging from 0 to −20 at an increment of 1 in the dimensionless units was applied, prior to the evolution of the domain structure, along the y-axis and the average strain along the same direction was calculated based on the phase-field method. Again, the periodic boundary conditions were adopted in the evolution calculations with the fixed dimensions. As mentioned above, under the condition of fixed dimensions, applied stresses are actually applied strains and the material response to the applied strains is a stress field. However, we convert the applied strains and the material-responded stresses to the applied stresses and the material-responded strains through Hooke's law to present the simulation results in a conventional manner. With applied mechanical loading, the total average strain including two parts. One part is given by $\varepsilon^{\mathrm{e}}_{yy} = S_{yykl}\sigma^{\mathrm{e}}_{kl}$, which is attributed the deformation of the background paraelectric material. The other average strain, $\langle\varepsilon^{0}_{yy}\rangle$, is linked to the material-responded stresses, as described in Section 3.4. Thus, the total average strain response to an applied load is given by

$$\left\langle \varepsilon^{\mathrm{total}}_{yy} \right\rangle = \varepsilon^{\mathrm{e}}_{yy} + \left\langle \varepsilon^{0}_{yy} \right\rangle. \quad (25)$$

Again, 2000 steps of evolution, which were sufficient at the time step of $\Delta t^* = 0.04$ for the simulated ferroelectric to reach the steady state, were conducted at each level of applied stress. During the simulations, we found that stress–strain curves during the first loading-unloading cycle were different, to some extent, from those during the second loading-unloading cycle and they were completely repeatable in further loading-unloading cycles. Therefore, we report here the stress–strain curves during the second loading-unloading cycle to understand the steady mechanical response of the simulated ferroelectric to applied compressive stresses. Fig. 7 shows the stress–strain curves for the loading and unloading processes, where the loading curve is indicated by sequences of points A–B–C–D and the unloading curve is indicated by sequences of points D–E–F–A. The corresponding domain structures at points A–F are illustrated in Figs. 8(a)–(f).

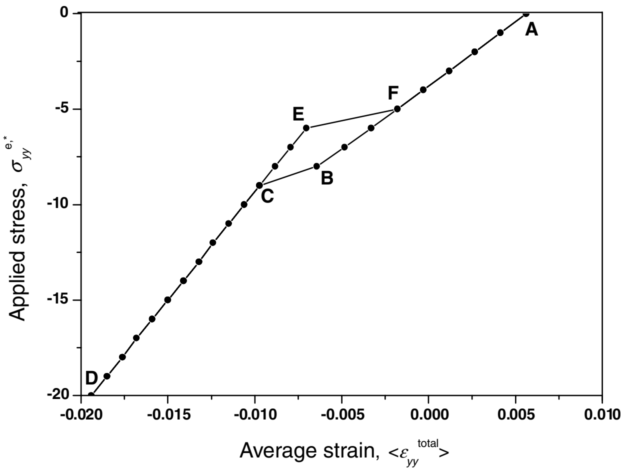

Fig. 7. Loading-rate-independent stress–strain curves.

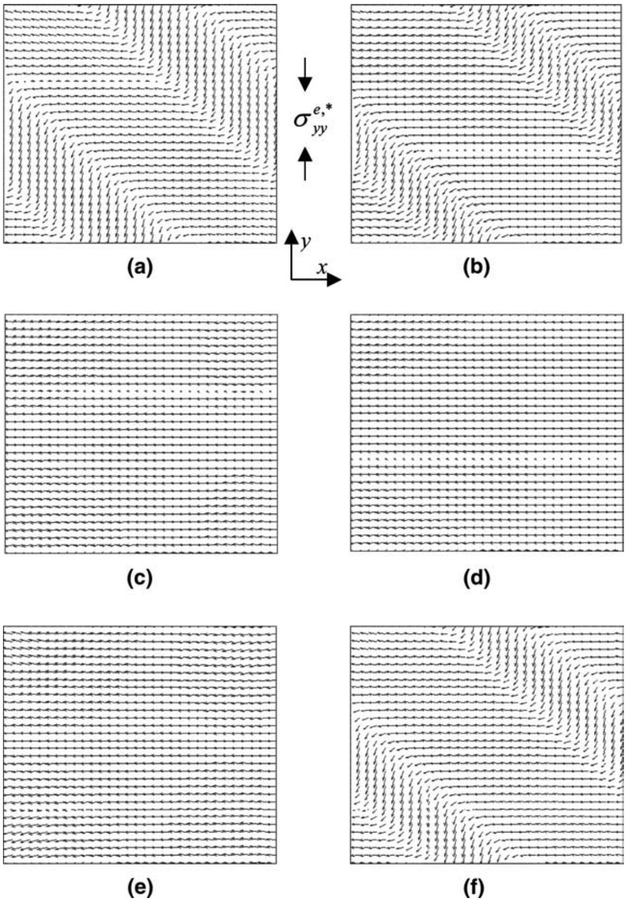

Fig. 8. Domain structures corresponding to points A–F in Fig. 7.

From point A to point B in Fig. 7, the applied stress, $\sigma^{\mathrm{e},*}_{yy}$, is linearly proportional to the average strain, $\langle\varepsilon^{\mathrm{total}}_{yy}\rangle$, and the slope of the applied stress over the average strain is 666.6, which represents the elastic stiffness of the simulated ferroelectric under simple compression. Figs. 8(a) and (b) indicate that when the compressive stress increases, domain walls move such that the domains parallel to the direction of the applied compressive stress shrink and the domains perpendicular to this direction grow. In addition to the domain wall motion, all dipoles in the domains parallel to the direction of the applied compressive stress rotate towards the direction perpendicular to the applied compressive stress. When the compressive stress increases its magnitude from −8 to −9, as marked by points B and C in Fig. 7, the average strain has a jump from -6.44×10^{-3} to -9.72×10^{-3}. This macroscopic strain jump is attributed to the change in the microscopic domain structure in which all domains with the original polarization direction parallel to the compressive stress direction disappear. Under this level of loading, all of the dipoles are parallel to the direction of the x-axis and form a single-domain structure, as shown in Fig. 8(c). The results indicate that the single-domain structure has a free energy lower than that in a polydomain structure when the magnitude of applied compressive stress is higher than a critical value. After the jump in the average strain, the applied stress, $\sigma_{yy}^{e,*}$, is linearly proportional to the average strain, $\langle \varepsilon_{yy}^{\text{total}} \rangle$, again and the slope of the applied stress over the average strain is 1136.4 in the CD region, which is larger than 666.6 in the AB region. The simulated ferroelectric has a single-domain structure in the CD region, as indicated in Figs. 8(c) and (d). Therefore, no domain wall motion is involved in the deformation of the simulated ferroelectric in the CD region. The most of the linear parts of the unloading curve coincide with the loading curve except the jump, at which the average strain jumps backwards from -7.03×10^{-3} to -1.79×10^{-3} when the load decreases from −6 to −5, as marked by points E and F in Fig. 7. Fig. 8(e) and (f) illustrate the corresponding domain structures. During the unloading process, the single-domain structure has a free energy higher than that in a polydomain structure when the magnitude of the applied compressive stress is lower than a critical value. However, the critical magnitude of the applied compressive stress causing the jump during unloading differs from that during loading. It is the jump difference during loading and unloading that forms the hysteresis loop, BCEF, in the stress–strain curves. The simulated ferroelectric changes its single-domain structure before the reverse jump to a polydomain structure after the reverse jump. The evolution from the single-domain structure to the polydomain structure was achieved by new domain nucleation and growth, which was revealed in the transient patterns of the domain structures, as shown in Fig. 9. Since Fig. 8 illustrates only steady domain structures, it does not show the detail of the new domain nucleation process. The polydomain structure at point F is similar to the structures at points A and B. Since the mechanical load at point F is higher than that at point A and lower than that at point B, the percentage of the domains with the polarization basically parallel to the y-axis at point F is smaller than that at point A, but larger than that at point B, as shown in Figs. 8(a), (b) and (f).

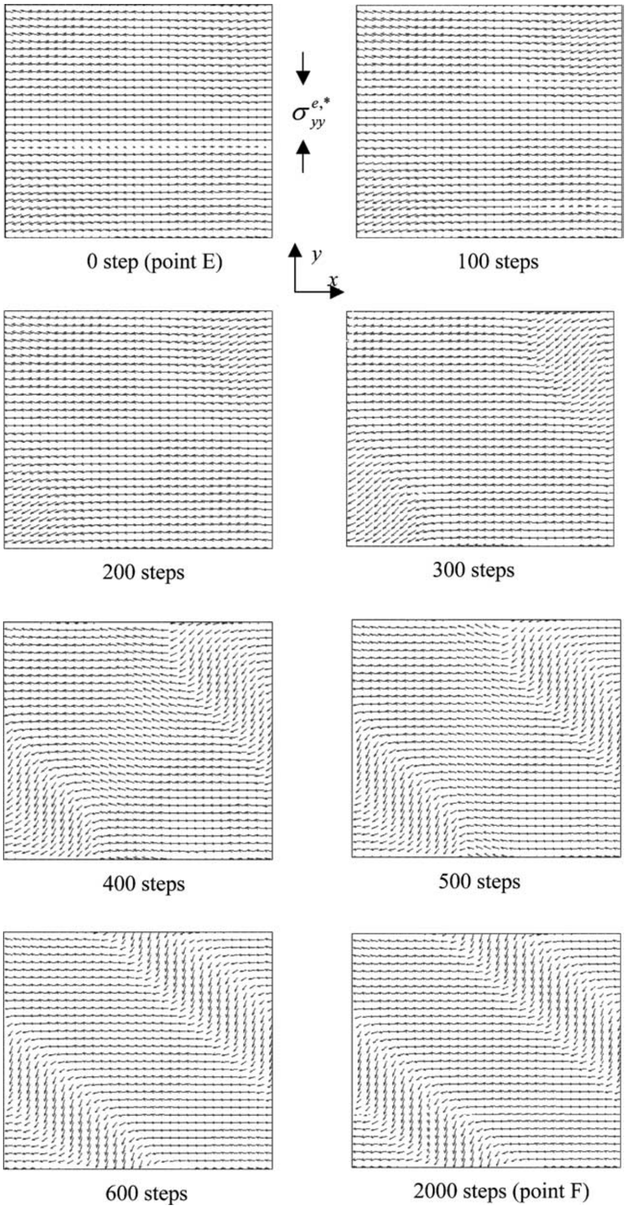

0 step (point E)

100 steps

200 steps

300 steps

400 steps

500 steps

600 steps

2000 steps (point F)

Fig. 9. Temporal evolution of polarization switching when the compressive stress decreased from −6 to −5.

As mentioned above, the elastic stiffness of the polydomain-structured ferroelectric is lower than that of the single-domain-structured ferroelectric. This is attributed to domain wall motion, which occurs in the polydomain-structured ferroelectric. Arlt et al. [41] and Fu and Zhang [42] have proposed that 90°-domain wall motion will generate mechanical deformation. In the 90°-domain wall kinetics model [42,43], the total elastic compliance, s, is attributed to volume and domain wall contributions, i.e., $s = s_V + s_D$, where the subscripts ‘V’ and ‘D’ denote volume and domain wall, respectively. The elastic stiffness, c, is the reciprocal of the elastic compliance, i.e., $c = 1/s = 1/(s_V + s_D)$. For the single-domain-structured ferroelectric, no domain wall motion occurs and the contribution from domain wall motion to elastic compliance is zero, i.e., $s_D = 0$. As a result, the elastic stiffness in the single-domain-structured ferroelectric, $c = 1/s_{\mathrm{V}}$, is larger than that in the multi-domain state, $c = 1/(s_{\mathrm{V}} + s_{\mathrm{D}})$. With the phase-field model, we are able to analyze qualitatively the contribution from the changes in polarizations including domain wall motion to the elastic compliance. Using Eqs. (24) and (25), the elastic compliances in the AB and CD regions are calculated by

$$s^{\mathrm{AB}} = \frac{\left\langle \varepsilon_{yy}^{\mathrm{total}} \right\rangle^{\mathrm{B}} - \left\langle \varepsilon_{yy}^{\mathrm{total}} \right\rangle^{\mathrm{A}}}{\left\langle \sigma_{yy}^{\mathrm{e}} \right\rangle^{B} - \left\langle \sigma_{yy}^{\mathrm{e}} \right\rangle^{\mathrm{A}}} = \frac{-S_{yykl}\left[\left\langle \sigma_{kl}^{(\mathrm{s})} \right\rangle^{\mathrm{B}} - \left\langle \sigma_{kl}^{(\mathrm{s})} \right\rangle^{\mathrm{A}}\right]}{\left\langle \sigma_{yy}^{\mathrm{e}} \right\rangle^{\mathrm{B}}} + S_{yyyy}, \tag{26a}$$

$$s^{\mathrm{CD}} = \frac{\left\langle \varepsilon_{yy}^{\mathrm{total}} \right\rangle^{\mathrm{D}} - \left\langle \varepsilon_{yy}^{\mathrm{total}} \right\rangle^{\mathrm{C}}}{\left\langle \sigma_{yy}^{\mathrm{e}} \right\rangle^{\mathrm{D}} - \left\langle \sigma_{yy}^{\mathrm{e}} \right\rangle^{\mathrm{C}}} = \frac{-S_{yykl}\left[\left\langle \sigma_{kl}^{(\mathrm{s})} \right\rangle^{\mathrm{D}} - \left\langle \sigma_{kl}^{(\mathrm{s})} \right\rangle^{\mathrm{C}}\right]}{\left\langle \sigma_{yy}^{\mathrm{e}} \right\rangle^{\mathrm{D}} - \left\langle \sigma_{yy}^{\mathrm{e}} \right\rangle^{\mathrm{C}}} + S_{yyyy}, \tag{26b}$$

respectively, where superscripts A, B, C, and D denote, correspondingly, points A, B, C, and D in Fig. 7. It should be noted that due to the excellent linearity in either the AB or the CD region, we may arbitrarily choose two points in the AB region or in the CD region without changing the result. Also, the excellent linearity in either the AB or the CD region yields a constant elastic compliance in each region. The first term on the right-hand side of Eq. (26a) or (26b) represents the contribution from the changes in polarizations to the elastic compliance and the second term on the right-hand side of Eq. (26a) or (26b) is a material constant, $S_{yyyy} = s_{11}^{*} = 7.909 \times 10^{-4}$ in the dimensionless units, used as an input datum in the present study. Thus, the contribution from the changes in polarizations to the elastic compliance must be a constant in each region because the elastic compliance in each region is a constant. Then, we can denote the first term on the right-hand side of Eq. (26a) or (26b) by $s^{\mathrm{p,AB}}$ or $s^{\mathrm{p,CD}}$ correspondingly, for simplicity. Moreover, a constant contribution from the changes in polarizations implies that the average stresses induced by polarization changes must be linearly proportional to the applied compressive stress, which is consistent with the prediction from the domain wall kinetics model [42,43]. From the simulated results, $s^{\mathrm{AB}} = 1.5 \times 10^{-3}$and $s^{\mathrm{CD}} = 8.8 \times 10^{-4}$, and the input datum, $s_{11}^{*} = 7.909 \times 10^{-4}$, we have $s^{\mathrm{p,AB}} = 7.0 \times 10^{-4}$ and $s^{\mathrm{p,CD}} = 0.909 \times 10^{-4}$. Clearly, the value of $s^{\mathrm{p,AB}}$ is much larger than the value of $s^{\mathrm{p,CD}}$, which is attributed to domain wall motion in the polydomain-structured ferroelectric. However, the nonzero value of $s^{\mathrm{p,CD}}$ indicates that in addition to domain wall motion, any changes in polarization will contribute to mechanical deformation, as indicated by Eq. (9). In the single-domain-structured ferroelectric, the polarizations vary with the applied compressive stress. Fig. 10 shows the changes in the average polarization components, $\langle P_x^{*} \rangle$ and $\langle P_y^{*} \rangle$, with applied compressive stress. The average polarization component,$\langle P_y^{*} \rangle$, is nonzero in the single-domain-structured ferroelectric, which is visible if one zooms-in in Figs. 8(c)–(e), but its magnitude is about five orders smaller than the magnitude of $\langle P_x^{*} \rangle$. Thus, the magnitude of the average polarization is determined by the magnitude of $\langle P_x^{*} \rangle$, which increases almost linearly with the applied compressive stress, as shown in Fig. 10. As a direct result, we may state that an applied compressive stress increases the magnitude of the average polarization of a single-domain-structured ferroelectric.

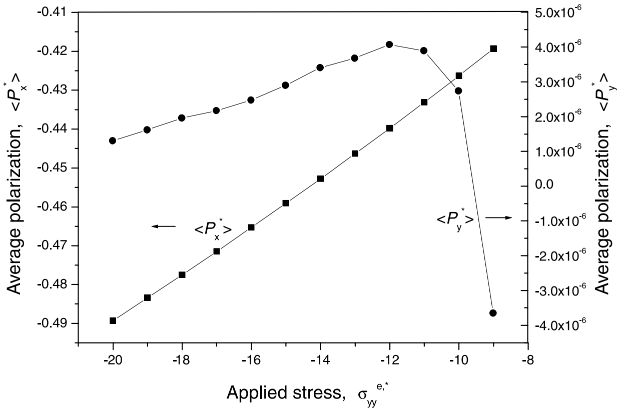

Fig. 10. Average polarizations versus applied compressive stress.

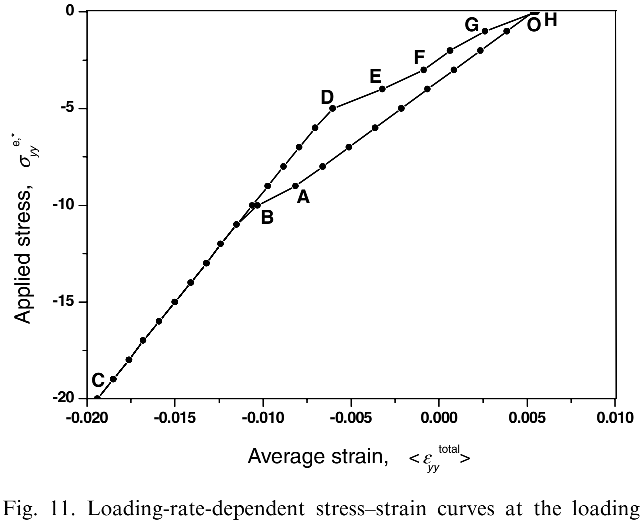

Fig. 11. Loading-rate-dependent stress–strain curves at the loading rate of 1/8.

3.5.2. Loading-rate-dependent behaviors

In this section, we report simulation results of the mechanical response of the average strain to applied stresses under two loading rates. We used the same simulation conditions as these described in Section 3.5.1 except that the total steps of evolution at each level of applied stress were set at 200 or 20, which corresponded to a loading-unloading rate of 1/8 or 10/8 in the dimensionless units for the time step of $\Delta t^* = 0.04$ and the stress increment of 1. Fig. 11 shows the stress–strain curves at the loading-unloading rate of 1/8, where the loading curve is indicated by sequences of points O–A–B–C and the unloading curve is indicated by sequences of points C–D–E–F–G–H. The initial domain structure at point O is the same as that shown in Fig. 3(a) and the domain structures corresponding to points A–H in Fig. 11 are shown as Figs. 12(a)–(h). Comparing Fig. 11 with Fig. 7 indicates that the area of the hysteresis loop in Fig. 11 is larger than that in Fig. 7. The jump magnitudes in the loading-rate-dependent stress–strain curves shown in Fig. 11, are correspondingly smaller than the jump magnitudes in the loading-rate-independent stress–strain curves shown in Fig. 7. At the loading rate of 1/8, the loading curve shows two linear regions, which are similar to the loading-rate-independent loading curve shown in Fig. 7, whereas the unloading curve reveals only one linear region, which differs from the unloading curve of two linear regions in Fig. 7. Clearly, the difference is caused by a fast loading rate, at which the simulated ferroelectric cannot reach a steady state at each level of loading. As expected, transitional domain structures appear in the dynamic loading-unloading process, as shown by Figs. 12(d)–(g), especially when new domain nucleation and growth occur during the unloading process. Figs. 12(d)–(g) seem to be similar to the transitional domain structures illustrated in Figs. 1(c)–(e). Therefore, we will not discuss Figs. 12(d)–(g) in detail for concise.

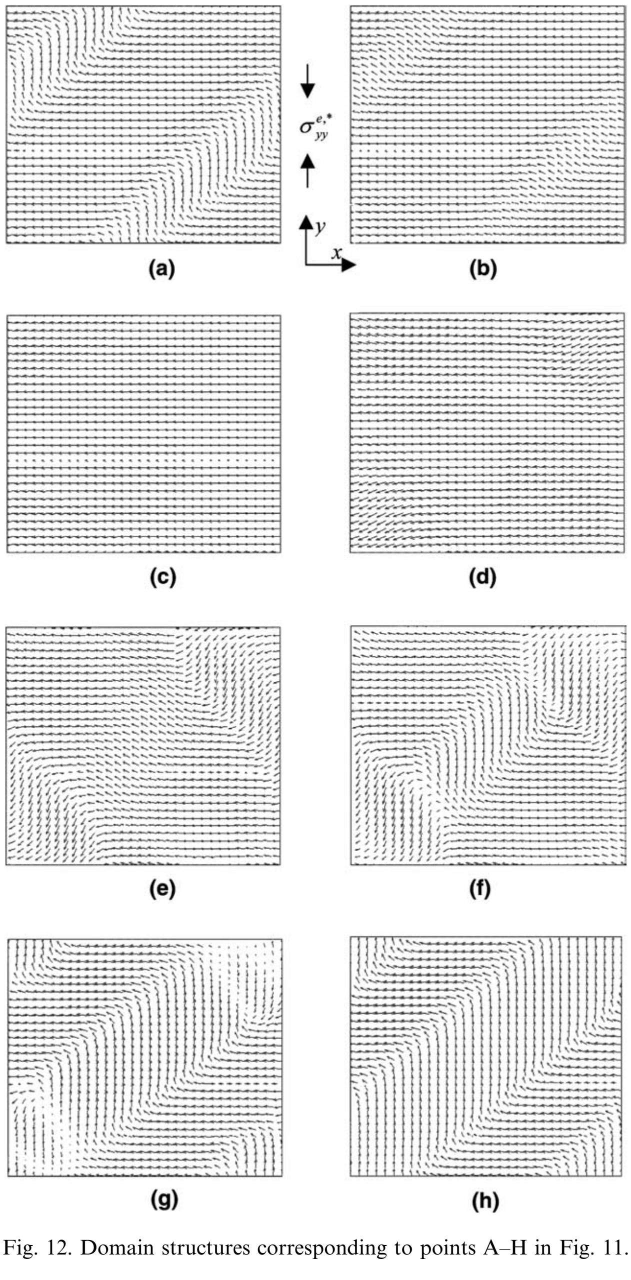

Fig. 12. Domain structures corresponding to points A–H in Fig. 11.

Increasing the loading rate further to 10/8 expands the hysteresis loop, as shown in Fig. 13. Fig. 13 indicates the loading-unloading curves at the loading rate of 10/8, where the loading curve is indicated by sequences of points A–B–C–D–E and the unloading curve is indicated by sequences of points E–D–F–G–H. The corresponding domain structures to points A–H are illustrated in Figs. 14(a)–(h). At the loading rate of 10/8, the jumps occurring in the loading-rate-independent stress–strain curves disappear and are replaced by smooth curves. When the load is completely released, the average strain cannot return to its original point, as

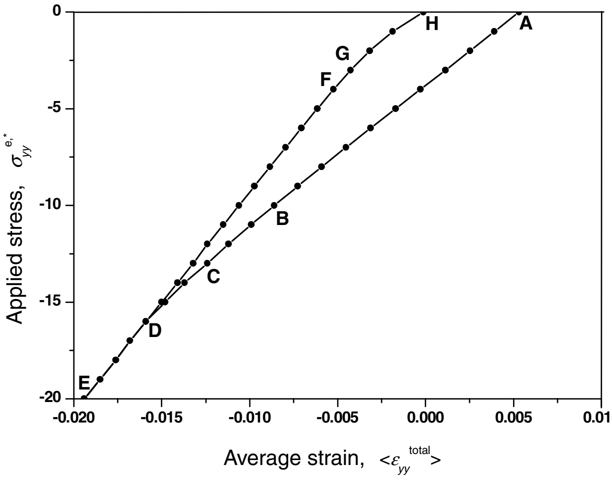

Fig. 13. Loading-rate-dependent stress–strain curves at the loading rate of 10/8.

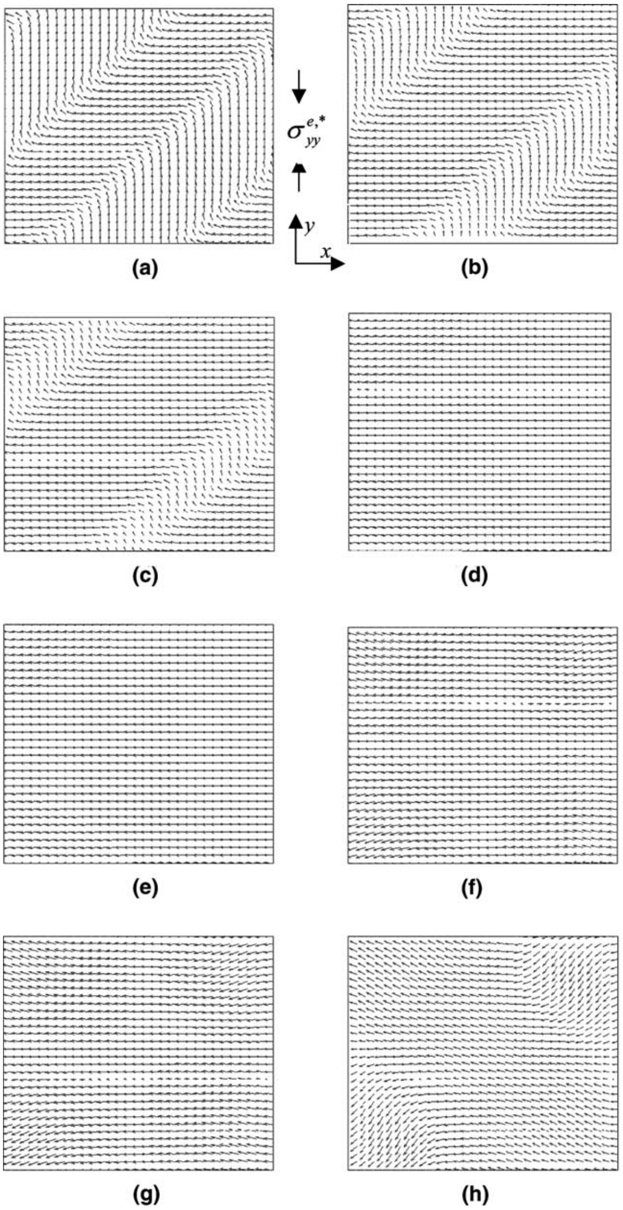

Fig. 14. Domain structures corresponding to points A–H in Fig. 13.

shown by point H in Fig. 13. Fig. 14(h) illustrates the domain structure, indicating that the new domains appear just at the left-bottom and right-top corners. Again, the loading curve reveals two linear regions and the unloading curve shows only one linear region at the loading rate of 10/8. As mentioned above, elastic constants can be determined from the linear regions. It is interesting to find that increasing the loading rate does not change the elastic compliances, but it extends both the high elastic compliance region during loading and the low elastic compliance region during unloading. The faster the loading-unloading rate is, the greater the extension will be. The result is expected because a fast loading-unloading rate shortens the time such that the domain structure cannot reach its steady state.

4. Concluding remarks

Phase-field simulations were conducted in the present work to understand the paraelectric–ferroelectric phase transformation, the material responses of a ferroelectric to external electric fields or mechanical stresses. The temporal evolution of polarizations shows that domain switching is a kinetic process of the disappearance of old domains and the nucleation and growth of new domains and the domain growth is accomplished through domain wall motion, i.e., partial domain switching. The applied electric fields can induce both 180°- and 90°-polarization switching. Although the applied stresses cause only 90°-polarization switching during the loading process, 180°-domain walls appear during the unloading process with new domain nucleation, as shown in Figs. 12(f) and (g). The simulation results confirm the analytic predictions from the domain wall kinetics model [42,43] that the macroscopic elastic compliance consists of two parts. One part of the elastic compliance is independent of polarizations and the other depends on polarizations. The polarization-linked compliance has two values, depending on that whether domain wall motion occurs. In a polydomain-structured ferroelectric, domain wall motion occurs and then results in a high value of the polarization-linked compliance, whereas in a single-domain-structured ferroelectric, applied stresses enhance the magnitude of polarizations and then yield a low value of the polarization-linked compliance. The simulation results demonstrate also that the loading rate plays an important role in the material responses to external fields. In summary, phase-field simulations indeed yield physical insights into the domain switching mechanism.

Acknowledgements

This work was supported by a grant (N_HKUST602/01) from the Research Grants Council of the Hong Kong Special Administrative Region, China. T.Y.Z. thanks the Croucher Foundation for the Croucher Senior Research Fellowship Award, which gave him more research time by releasing him from teaching duties. S.Q.S. was also partially supported by a grant (G-T921) from Hong Kong Polytechnic University.

References

[1] Chen PJ, Tucker TJ. Int J Eng Sci 1981;19:147.
[2] Huo Y, Jiang Q. Int J Solids Struct 1998;35:1339.
[3] Arlt G. Ferroelectrics 1996;189:103.
[4] Arlt G, Calderwood JH. Appl Phys Lett 2002;81:2605.
[5] Fan J, Stoll WA, Lynch CS. Acta Mater 1999;47:4415.
[6] Fulton CC, Gao H. Acta Mater 2001;49:2039.
[7] Hwang SC, Waser R. Acta Mater 2000;48:3271.

[8] Hwang SC, Lynch CS, McMeeking RM. Acta Metall Mater 1995;43:2073.

[9] McMeeking RM, Hwang SC. Ferroelectrics 1997;200:151.

[10] Huber JE, Fleck NA, Landis CM, McMeeking RM. J Mech Phys Solids 1999;47:1663.

[11] Hwang SC, McMeeking RM. Ferroelectrics 1998;211:177.

[12] Hwang SC, McMeeking RM. Int J Solids Struct 1999;36:1541.

[13] Michelitsch T, Kreher WS. Acta Mater 1998;46:5085.

[14] Lu W, Fang DN, Hwang KC. Theor Appl Fract Mech 2001;37:29.

[15] Lu W, Fang DN, Hwang KC. Theor Appl Fract Mech 2001;37:39.

[16] Lu W, Fang DN, Li CQ, Hwang KC. Acta Mater 1999;47:2913.

[17] Landis CM. J Mech Phys Solids 2003;51:1347.

[18] Chen LQ, Wolverton C, Vaithyanathan V, Liu ZK. MRS Bulletin 2001;(March issue):197.

[19] Artemev A, Wang Y, Khachaturyan AG. Acta Mater 2000;48:2503.

[20] Wu K, Morral JE, Wang Y. Acta Mater 2001;49:3401.

[21] Katamura J, Sakuma T. Acta Mater 1998;46:1569.

[22] Cha PR, Kim SG, Yeon DH, Yoon JK. Acta Mater 2002;50:3817.

[23] Rodney D, Bouar YL, Finel A. Acta Mater 2003;51:17.

[24] Shen C, Wang Y. Acta Mater 2003;51:2595.

[25] Cao W, Tavener S, Xie S. J Appl Phys 1999;86:5739.

[26] Ahluwalia R, Cao W. J Appl Phys 2003;93:537.

[27] Cao W, Cross LE. Phys Rev B 1991;44:5.

[28] Nambu S, Sagala DA. Phys Rev B 1994;50:5838.

[29] Yang W, Chen LQ. J Am Ceram Soc 1995;78:2554.

[30] Hu HL, Chen LQ. Mater Sci Eng A 1997;238:182.

[31] Hu HL, Chen LQ. J Am Ceram Soc 1998;81:492.

[32] Gao YF, Suo Z. J Appl Mech 2002;69:419.

[33] Li YL, Hu SY, Liu ZK, Chen LQ. Appl Phys Lett 2001; 78:3878.

[34] Li YL, Hu SY, Liu ZK, Chen LQ. Acta Mater 2002;50:395.

[35] Li YL, Hu SY, Liu ZK, Chen LQ. Appl Phys Lett 2002;81:427.

[36] Ahluwalia R, Cao W. J Appl Phys 2001;89:8105.

[37] Ahluwalia R, Cao W. Phys Rev B 2000;63:012103.

[38] Khachaturyan AG. Theory of structural transformations in solids. New York: Wiley; 1983.

[39] Mura T. Micromechanics of defects in solids. Boston: Kluwer Academic Publishers; 1987.

[40] Li Z, Foster M, Dai XH, Xu XZ, Chan SK, Lam DJ. J Appl Phys 1992;71:4481.

[41] Arlt G, Dederichs H, Herbiet R. Ferroelectrics 1987;74:37.

[42] Fu R, Zhang TY. Acta Mater 2000;48:1729.

[43] Zhang TY, Zhao MH, Tong P. Adv Appl Mech 2002;38:147.